Journal of Power Sources 196 (2011) 8484–8493

Contents lists available at ScienceDirect

Journal of Power Sources

journal homepage: www.elsevier.com/locate/jpowsour

Measurement of the clamping pressure distribution in polymer electrolyte fuel cells using piezoresistive sensor arrays and digital image correlation techniques

R. Montanini[a,*], G. Squadrito[b], G. Giacoppo[b]

[a] Department of Industrial Chemistry and Materials Engineering, University of Messina, Italy
[b] CNR Institute for Advanced Energy Technologies "Nicola Giordano", Messina, Italy

ARTICLE INFO

Article history:
Received 14 January 2011
Received in revised form 19 May 2011
Accepted 3 June 2011
Available online 12 June 2011

Keywords:
PEFC fuel cells
Contact pressure distribution measurement
Clamping torque
Piezoresistive thin-film sensor arrays
Digital image correlation (DIC)

ABSTRACT

A combined method for the simultaneous measurement of the clamping pressure distribution and endplates deformation in polymer electrolyte fuel cells (PEFC) is presented. The proposed approach, which allows overcoming some important limitations associated with the use of conventional pre-scaled pressure films, is used to investigate the correlation between the actual pressure distribution on the membrane electrode assembly (MEA), the endplate out-of-plane deformation and the applied clamping torque, for two single fuel cells assembled with either copper or aluminium/copper endplates. Results proved that, in point-load design PEFCs, both pressure magnitude and distribution are affected by endplates deformation and thickness mismatching between the sealing gasket and the MEA. Moreover, while the average pressure on the MEA displays a slight increase (+25%) as the clamping torque is raised from 5 to 10 N m, it increases monotonically on the sealing gasket, with local peaks that exceed the saturation level of the sensor array (20.7 MPa). A dimensionless uniformity index has been introduced to assess the uniformity of the pressure distribution, allowing an easy comparison of different fuel cell assembly configurations. The proposed methodology might assist the design of next-generation fuel cells or could be used as a powerful validation tool for detailed finite element models. It can also be applied to study other kind of fuel cells and batteries as well.

1. Introduction

Polymer electrolyte fuel cell (PEFC) is an electrochemical device that converts the chemical energy stored in hydrogen and oxygen into electricity, without generating pollutants. A conventional PEFC (Fig. 1) basically consists of two polar plates with multiple serpentine flow fields and a membrane electrode assembly (MEA) inserted between them. Highly conductive collectors are used to drive the dc current, whereas rigid endplates are employed as part of the clamping system to provide compressive force in order to bundle the single fuel cells together to form a stack. Due to their low operation temperature (60–100 °C) and quick start up and shut down, PEFCs are thought to be the major candidate as future energy suppliers for transportation and residential applications. For these reasons, PEFCs are undergoing intense development and today are considered close to the commercialisation threshold. However, additional improvement of performance, efficiency, reliability, manufacturability and cost effectiveness is still considered a critical challenge in PEFC development. In this context extensive research has been carrying out in order to get a complete understanding of PEFC basic mechanisms and to assess the influence of critical parameters affecting their performance and durability.

PEFC performance depends on voltage losses primarily caused by three main sources: activation, ohmic and concentration polarisation [1]. Both interfacial electric contact resistances and mass transport limitations are influenced by the cell assembly mechanism which governs the resulting force distribution acting on the membrane electrode assembly of the fuel cell. For this reason many scientific works have been devoted to the study of the interaction between the bipolar plate, hosting the flow field channels for reactant supply and exhaust removal, and the gas diffusion layer (GDL) covering the electrode assembly. Since an uneven distribution of the contact pressure on the active layer will result in hot spots which may have a detrimental effect on PEFC electrochemical performance and life [2–4], ensuring a proper and uniform pressure

* Corresponding author at: Department of Industrial Chemistry and Materials Engineering, University of Messina, Faculty of Engineering, Contrada di Dio, I-98166 Messina, ME, Italy. Tel.: +39 90 397 7248; fax: +39 90 397 7464.
E-mail addresses: rmontanini@ingegneria.unime.it (R. Montanini), gaetano.squadrito@itae.cnr.it (G. Squadrito), giosue.giacoppo@itae.cnr.it (G. Giacoppo).

0378-7753/$ – see front matter © 2011 Elsevier B.V. All rights reserved.
doi:10.1016/j.jpowsour.2011.06.017

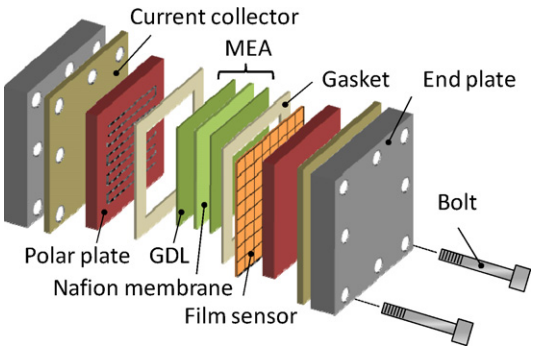

Fig. 1. Schematic drawing of a single polymer electrolyte membrane fuel cell.

distribution between mating surfaces is one of the most important goals in fuel cell design.

For a given stacking design, contact pressure levels are usually controlled by applying an appropriate clamping pressure on the endplates by means of distributed pairs of nuts and bolts (point-load design). An insufficient clamping pressure may result in sealing problems, such as fuel leakage, internal crossover and high contact resistance between the GDL and the bipolar plates. On the other hand, a high clamping pressure may squeeze the relatively thin gas diffusion layer and change its porosity and permeability, choking the flow of gases and making the migration of water difficult.

Experimental investigations to map pressure distribution within PEFC are usually performed by using pressure sensitive films. This measurement technique is based on thin film with uniformly distributed ink filled micro-capsules that progressively break under load releasing the ink. Pressure magnitude is easily determined by comparing the intensity variations to a colour correlation chart, in a similar way to interpreting litmus paper.

Using this technique, Lee et al. [2] studied the effects of GDL compression on the performance of a 10 cm^2 PEFC with four-bolt clamping configuration. Three types of gas diffusion layers were evaluated at fixed stoichiometric flow rates, with bolt torques of 11.3, 14.1 and 16.9 N m, respectively. A Pressurex™ sensitive film was placed between the MEA and the GDL but, for each torque level, only the average pressure was reported. Besides, since the same gasket was always used for the experiments, the values obtained for the average pressure showed a strong dependence on GDL thickness, which varied from 0.2 to 0.5 mm.

Wang et al. [3] used pressure sensitive Fuji films inserted between the bipolar plate and the diffusion layer of a 25 cm^2 PEFC to measure the pressure distribution of both conventional and newly designed hydro-pressurized endplates. It was found that by pressurizing the built-in pocket with hydraulic fluid, the pressure distribution over the fuel cell active area can be improved and fuel cell performance enhanced. The study was focused on the comparison between conventional and newly designed endplates rather than on the evaluation of pressure distribution changes produced by different clamping torques. Furthermore, due to saturation of the pressure film, the obtained images suffered for low contrast, preventing pressure variations on the active area to be accurately measured.

Recently, in a comprehensive study Wen et al. [4] reported a systematic statistical analysis to investigate the effects of various combinations of bolt configuration and clamping torque on the performance and relevant electrode kinetic parameters of a single rectangular PEFC (active area of 100 cm^2) and a 10-cell stack. Pressure sensitive films were used in the experiments to visualize the contact pressure distributions under three different clamping torques (8, 12 and 16 N m) and three different bolt configurations (2, 4 and 6 bolts). The uniformity of the contact pressure distribution, the ohmic resistance and the mass transport limit current showed highly linear correlations with the mean contact pressure for the single cell, while this was not the case for the 10-cell stack, where clear cell-to-cell variations were observed for both cell mean contact pressure and pressure fluctuation intensity.

Lee et al. [5] used finite element analysis (FEA) to simulate the cell stack assembly of a single PEFC with Al 5052 flow field plates. Contours of pressure distribution and compliance were obtained for key components such as the MEA and the GDL. In order to verify the results of the numerical analysis, experimental tests using a pre-scale Fuji film placed between the flow field plate and the MEA were conducted to establish the actual pressure distribution at four different clamping pressure levels. The calculated pressure distributions were found to be qualitatively similar to the experimental ones, but the percentage error between measured and simulated pressures, computed by averaging the values on nine different squares evenly distributed over the contacting surface, was quite large (10–60%). Moreover, the use of pre-scale pressure films, that saturate as the maximum pressure had been reached, did not allow pressure relaxations to be measured as the clamping pressure changed, thus hiding important information.

Numerical simulation has also been used to estimate the effect on PEFC performance of either fuel cell contact resistance [6,7] or GDL porosity [8] and to identify the effect of assembly parameters on the MEA pressure distribution by means of a robust design analysis based on response surface methodology [9]. Unfortunately, not all the numerical models presented in literature have been validated experimentally.

Another approach is that used by Chang et al. [10], who measured several electro-physical properties (i.e., porosity, gas permeability, electrical resistance and thickness) of a carbon paper gas diffusion layer using a special designed test rig. Empirical correlations for the gas permeability and the electrical resistance of the GDL were found in terms of the clamping pressure level. Results showed that a low clamping pressure (<5 bar) leads to a high interfacial resistance between the bipolar plate and the gas diffusion layer that reduces the electrochemical performance of the fuel cell. In contrast, a high clamping pressure (>10 bar) reduces the contact resistance between the graphite plate and the gas diffusion layer, but meanwhile narrows down the diffusion path for mass transfer from gas channels to the catalyst layers. However, the experimental tests were carried out on a test stand simulating the actual behaviour of a PEFC and no information about the internal contact pressure distribution was provided.

To overcome these limitations the authors started a research [11,12] aimed at developing a consistent method to measuring simultaneously both the contact pressure distribution and the endplate deformation, allowing real-time continuous data acquisition as the clamping pressure is varied. The proposed methodology is based on the use of a distributed piezoresistive array sensor for the measurement of the contact pressure distribution on the MEA and on full-field digital image correlation for the assessment of endplates deformation. Following a detailed description of the proposed measurement technique and its calibration against reference standards, the present paper reports and discusses the results obtained by performing experiments on two 25 cm^2 single PEFCs with copper and copper/aluminium endplates, respectively. One important goal of this study was to investigate the effect of the endplate stiffness on the actual pressure distribution: for this reason, the same gasket, MEA and flow field plates were used to compare the experimental results between the two cells. Another important task has been the assessment of the correlation existing between the pressure distribution on the MEA and the clamping torque used to seal the cell.

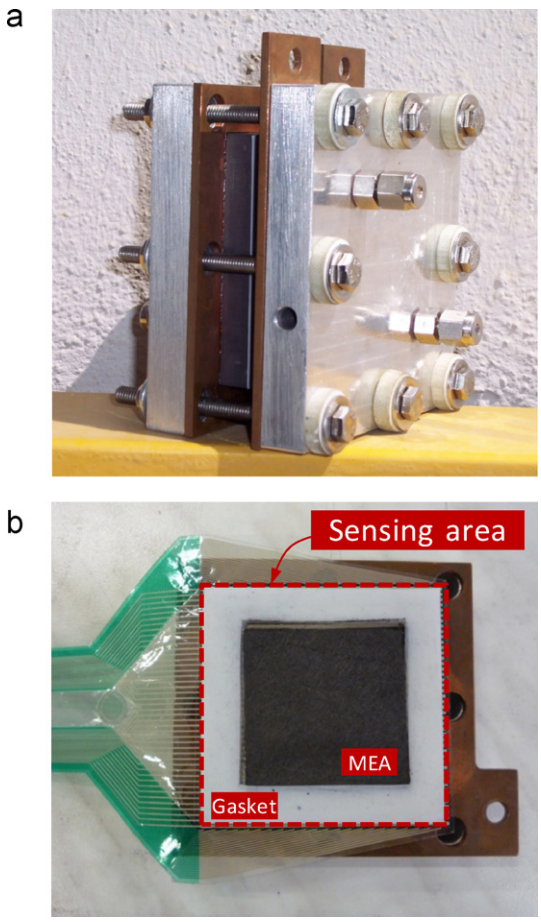

Fig. 2. PEFC with aluminium endplates and copper current collectors used to carry out the experimental tests: (a) assembled fuel cell; (b) embedding of the sensor array into the fuel cell.

2. Materials and methods

The PEFC (Fig. 2a) used to carry out the experimental tests was designed and assembled at the CNR-ITAE Institute. It has a multiple composite graphite serpentine flow field with an active area of 25 cm^2. The MEA consists of an assembly made of two 0.30 mm thick carbon paper gas diffusion layers (GDL) and two catalyst layers, hot pressed on a Nafion membrane; 0.3 mm thick PTFE gaskets were used for sealing. The total area of the graphite plate is 80 mm × 80 mm. The different components of the fuel cell are clamped together by means of two square endplates, having dimension of 110 mm × 110 mm, and 8 × M6 steel bolts. The endplates are either made of a 15 mm thick aluminium block with 3 mm thick copper current collectors (Al25) or a single 13 mm thick copper block (Cu25). Otherwise the assembly mechanism was the same for the two fuel cells.

Experimental tests were carried out by varying the external clamping pressure on the endplates step by step. This was obtained by using a calibrated torque wrench with torque values ranging from 5 to 10 N m, with 1 N m increments. At each step, after waiting for about 30 s, the torque value on each bolt was checked to account for possible gaskets or membrane electrode relaxations. The eight bolts were clenched in a cross configuration using always the same sequence (mid-left, mid-right, mid-lower, mid-upper, upper-left, lower-right, lower-left, upper-right). To avoid rigid body movements during the clamping procedure, one of the fuel cell endplates was fastened on a table by means of a mechanical vice. Levelling of the assembly was also accurately verified using a digital inclinometer. Measurements were taken waiting 180 s after each step increase or decrease and repeated three times to check for repeatability.

2.1. Pressure distribution measurements

Digital piezoresistive sensor arrays (Tekscan, Inc., South Boston, MA, USA) were used to perform real-time measurements of the contact pressure distribution within the PEFC as the clamping torque is varied. Tekscan sensor arrays are thin (0.1 mm) flexible grid-based devices, consisting of a matrix of rows and columns of a patented semi-conductive ink coating that changes its electrical resistance when force is applied to it. These rows and columns intersect to form sensing elements (sensels) that are sandwiched between two flexible polyester sheets. The pressure on each element is assumed to be constant and equal to the pressure measured at the centre where the piezoresistive strips cross. By electronically scanning and measuring the change in resistance at each individual sensing element, the timing, force and location of contacts on the sensor surface can be determined. Raw (uncalibrated) output can be exported as a 8-bit b/w image.

A square 83.8 mm × 83.8 mm array (mod. #5076-3000) was used to perform the experimental tests. This sensor has 1936 sensing elements with spatial density of 27.6 sensel cm^{-2} (corresponding to a spatial resolution of 1.90 mm × 1.90 mm). The pressure saturation rating (P_{sat}) given by the manufacturer is 20.7 MPa, which leads to a minimum pressure resolution of about 80 kPa.

The sensor array was embedded into the fuel cell between the MEA and the graphite plate (Fig. 1), covering the electrode assembly as well as the gasket frame (Fig. 2b). A circular hole (which is visible on left of Fig. 2b) was practiced outside of the sensing area, nearby the electrical connections. This allowed the insertion of the central clamping bolt after folding up the film sensor. Some tests were also performed by removing the MEA and the gaskets, and placing the sensor matrix between the two flow-field plates.

2.1.1. Calibration of the sensor array

Sensor arrays coming from purchaser are not equilibrated and calibrated, so that equilibration and calibration of the matrix sensels must be performed in order to obtained quantitative data. These operations were carried out by designing a pneumatic calibration device which allows applying uniform static pressure levels over the whole sensor area.

The calibration device, see Fig. 3a and b, consists of two flat and thick metal plates (planarity tolerance ±5 μm). The film sensor was first placed onto the bottom plate (Fig. 3c) and covered with a thin (0.01 mm) sheet of Teflon. Sealing was achieved by means of Gore-Tex™ gaskets placed over the deformable membrane. An air chamber was finally obtained by interposing a rigid polycarbonate spacer frame between the two stainless steel plates, which were clamped together by 12 × M10 bolts. The pressure into the air chamber was controlled by a pressure regulator, while a 0.05% accuracy class digital pressure transducer (AEP Transducers, Modena, Italy), with resolution of 0.2 kPa, was used as reference meter. Finally, to allow entrapped air to be driven out from the sensor compartment, two holes were practiced into the bottom plate. An important feature of the realized calibration device is that compliances of mating surfaces are very similar to those of a conventional fuel cell, thus avoiding the introduction of systematic errors in the sensor response due to spatial filtering effects.

Before calibration, the sensor array was normalized to compensate for small differences in sensitivity between the sensels forming the measuring grid. The sensor was first placed into the calibration device and subjected to a uniform pressure load. Then a digital compensation was performed by acting on the gain of each

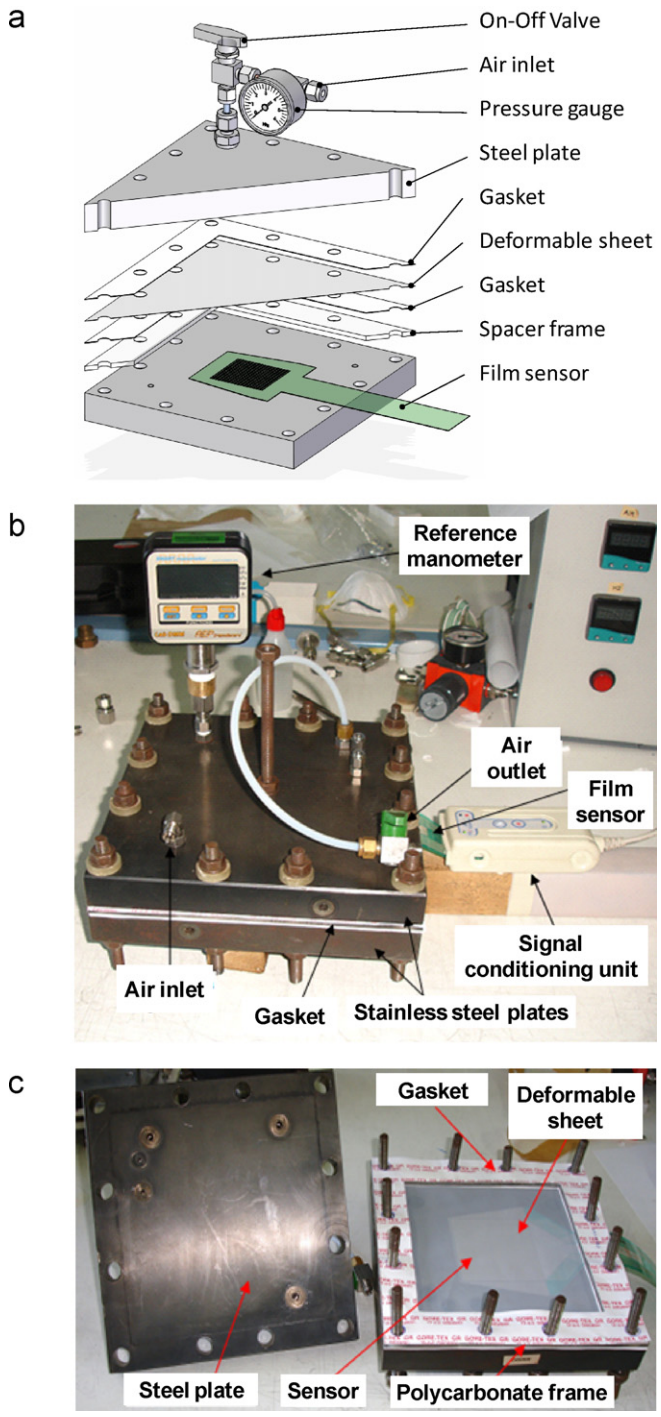

Fig. 3. Static calibration of the sensor array: (a) schematic drawing of the pneumatic calibration device; (b) view of the pneumatic calibration device with reference pressure meter; (c) detail of the air chamber with the sensor array inserted in it.

individual sensel, so that its digital level (DL) matched the average digital level of all loaded sensels. The equilibration process was repeated at multiple uniform pressure levels to ensure a consistent sensor response over the whole range of interest. After equilibration, the array showed, under a uniform pressure of 1000 kPa, a residual standard deviation of ±48 kPa (±1.3 DL) over the whole loaded area (Fig. 4). This value actually represents the lowest measurement uncertainty achievable using the current calibration device.

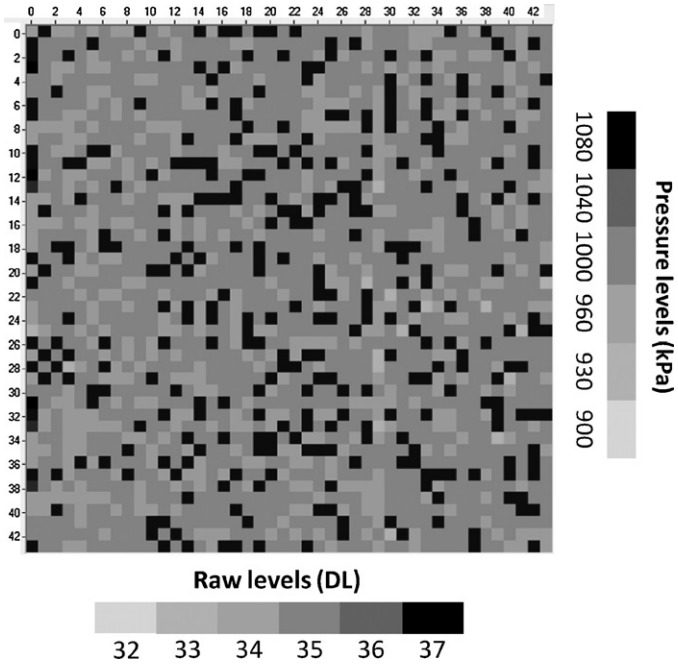

Fig. 4. Sensor array equilibration (total sensing area 83.8 mm × 83.8 mm, single sensel area 1.90 mm × 1.90 mm): raw (grey levels) and calibrated (kPa) response under a uniform pressure load of 1000 kPa after digital compensation (the scale of the figure was greatly compressed to allow small differences in sensels response to be highlighted).

Static calibration of the sensor array was carried out with both increasing and decreasing pressure steps in the 0–2000 kPa range. All tests were performed at 25 ± 2 °C ambient temperature. Throughout calibration, pressures were ramped up over 10 s (20 kPa s^{-1}) and held on for about 5 s. The calibration test was repeated six times in order to assess repeatability. At each uniform pressure stage the digital output of the array was averaged over all the matrix sensels to get the average raw output (Table 1). Repeatability under increasing pressures resulted better than 3% of the average raw output. For the range of pressures considered in the present study, reversibility tests did not highlight significant hysteresis effects (Table 1). Long term stability of the sensor array was also checked: after 10 h at uniform pressure, the sensor response exhibited a total drift of 74 kPa (2 DL), which is close to its resolution (80 kPa).

Average raw outputs were interpolated using a least squares curve-fitting technique. The sensor array exhibited a markedly nonlinear trend (Fig. 5), that can be well approximated by a third-order polynomial (R^2 = 0.999).

Table 1
Sensor array calibration: average measured output (8-bit raw) under increasing (+) and decreasing (−) pressure loads (DL = digital levels).

Ref. press. (kPa)	Raw (+) (DL)	Std. dev. (DL)	Std. dev. (%)	Raw (−) (DL)	Δ[a] (DL)
200	8.9	0.2	2.1	9.6	−0.7
400	16.9	0.5	2.9	17.5	−0.6
600	23.9	0.6	2.7	24.5	−0.6
800	29.4	0.7	2.4	30.2	−0.8
1000	34.9	0.8	2.2	35.5	−0.6
1200	40.3	0.9	2.3	41.0	−0.7
1400	44.9	0.8	1.8	45.7	−0.8
1600	49.1	1.0	2.1	49.9	−0.8
1800	53.1	1.1	2.1	53.9	−0.8
2000	57.1	1.1	1.9	57.1	0.0

[a] Difference between raw values under increasing and decreasing pressure loads.

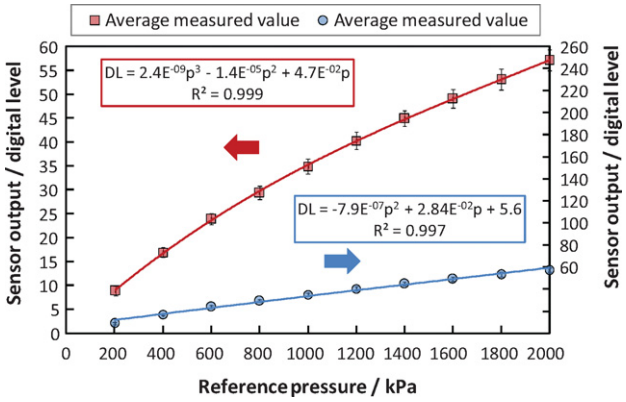

Fig. 5. Sensor array calibration: average raw output ± standard deviation (95% confidence level) measured at 10 different pressure levels. Experimental data were interpolated using either third-order polynomial curve-fitting (0–2000 kPa, upper curve/left scale) or second-order polynomial curve-fitting (0–20,700 kPa, bottom curve/right scale).

Following equilibration and calibration, the sensor was subjected to three loading cycles consisting of ten loads between 200 kPa and 2000 kPa applied in a random order. The sensor remained unloaded for 180 s between load applications. Pressure data were saved as raw values and calibrated externally by using the third-order interpolation curve. The root mean square (RMS) error between the calibrated sensor output and the reference pressure load was found to be 42 ± 7 kPa, corresponding to 2.1% of full scale.

While pressure levels measured on the MEA for various fuel cell configurations and clamping torques are well within the calibration range (0–2000 kPa), on the gasket they can locally result significantly higher. This does not represent a severe limitation since the exact knowledge of the contact pressure magnitude on the gasket is of secondary importance in this study, where we are mainly interested in assessing the pressure magnitude and distribution on the active area of the fuel cell. In order to convert digital levels into pressure values outside of the calibration range, some assumption must be made to perform the extrapolation. The solution here adopted relies on forcing the regression curve to pass through the sensor array full scale point, having coordinates 255 DL and 20700 kPa, respectively. This new (second order) regression curve (R^2 = 0.997) was then used to scale pressure levels higher than 2000 kPa (Fig. 5, bottom curve), while still using the formerly obtained calibration curve for pressure levels below 2000 kPa in order to keep the calibration accuracy very high in the 0–2000 kPa range.

2.2. Endplate out-of-plane deformation measurements

Endplates out-of-plane deformation was measured at different clamping torques using an optical full-field measurement technique (DIC, Digital Image Correlation) based on the comparison between digital images recorded in the un-deformed (or reference) and deformed states, respectively. The DIC approach relies on random speckle patterns sprayed onto the endplate surface which deforms together with it and acts as a carrier of deformation information. This random grey intensity distribution was created using opaque black paint deposited over a matt white uniform layer (Fig. 6a).

The DIC principle can be illustrated synthetically as follows. As shown in Fig. 6b, a subset of $(2M+1)\times(2M+1)$ pixels centred at point (x_0,y_0) from the reference image is first chosen and used to determine its corresponding location in the deformed image. A sum-square difference (SSD) correlation algorithm is then used to evaluate the similarity between the reference subset and the target subset. The matching procedure is carried out numerically through searching the peak position of the correlation coefficients distribution. Once the maximum correlation coefficient has been detected, the target subset in the two images can be determined, allowing the displacement field to be calculated.

In order to measure the out-of-plane component of the displacement vector, a stereo vision setup had to be used for tracking the motion of each image point in the field of view. The experimental setup hence consists of two high resolution (1624 × 1236 pixels) digital cameras equipped with 12 mm lens and two white light LED illuminators (Fig. 7a). The Aramis™ software (Gom GmbH, Braunschweig, Germany) was employed to carry out the correlation.

2.2.1. Calibration of the vision system

The use of a complex stereo setup (which was compulsory in order to measure the out-of-plane displacement component of the fuel cell endplate) required a preliminary calibration to determine the cameras configuration (distance and orientation) as well as the image characteristics of the lenses (e.g. focus, lens distortions). The measuring volume was calibrated using a ceramic calibration panel with coded reference markers and scale bars, determining

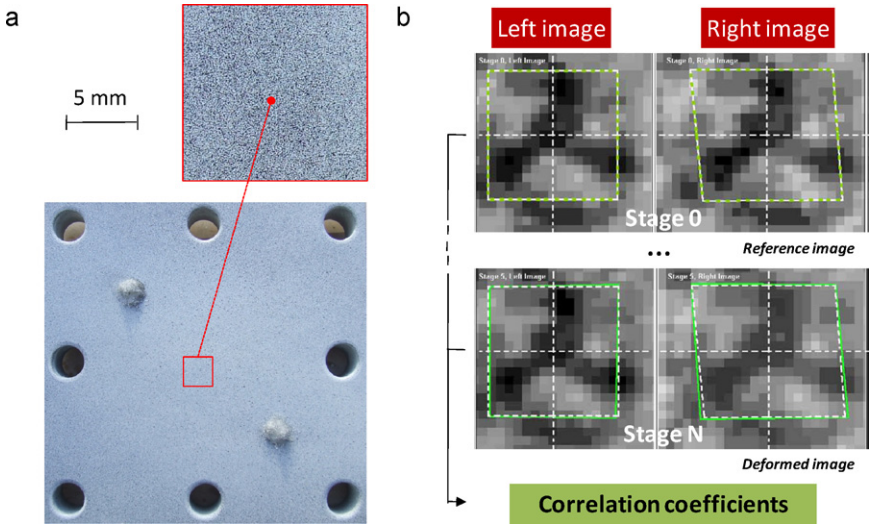

Fig. 6. Endplate out-of-plane displacement field measurements: (a) creation of a random grey intensity pattern onto the endplate surface; (b) measuring principle of 3D digital image correlation.

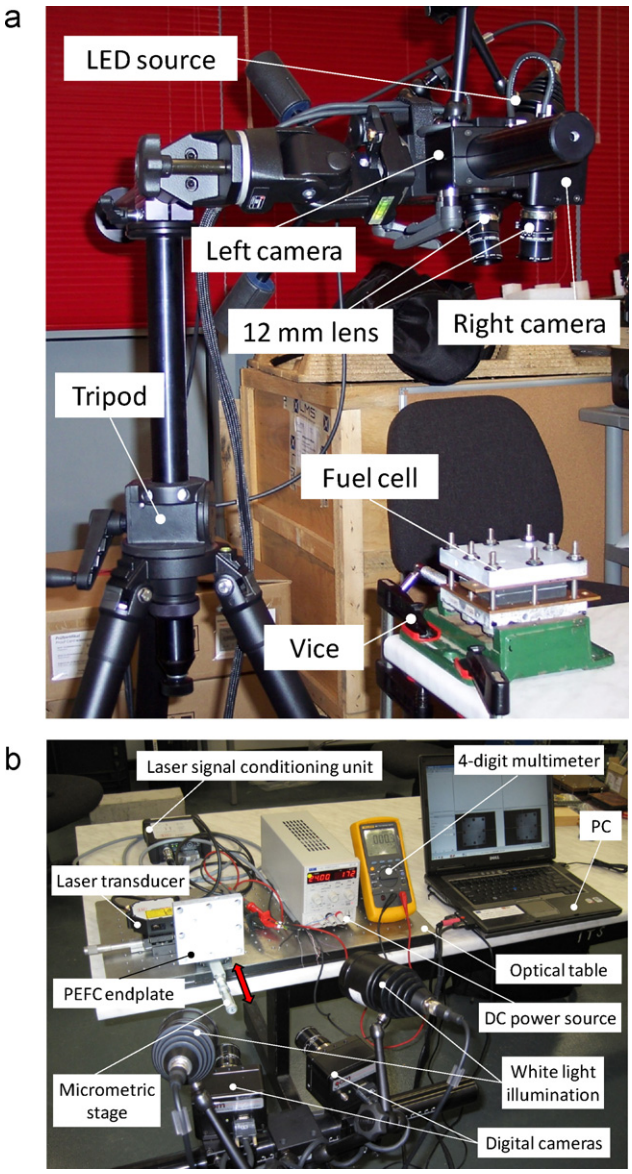

Fig. 7. Endplate out-of-plane displacement field measurements: (a) experimental set-up; (b) calibration of the vision system.

the 3D coordinates of the reference points in the 2D camera image. Reference point deviation (intersection error) was typically less than 0.1 pixels.

To assess the measurement uncertainty achievable with the current experimental setup, additional tests were carried out by fastening the endplate of the fuel cell on a translational micro-stage actuator mounted onto an optical table (Fig. 7b). A laser transducer (mod. ILD 2200-20, Micro-Epsilon, Ortenburg, Germany) with ±1 μm accuracy and 0.3 μm resolution and a 4-digit digital multimeter were used as reference for the measurement of the imposed out-of-plane displacement. Calibration tests were carried out in the 0–120 μm range, with 10 μm step increments. For each step, ten couples of images were recorded and used to compute the displacement by digital image correlation over a region of interest of about 4 cm^2 (further experiments performed by the authors changing the dimension of the region of interest did not evidenced systematic effects). The obtained results are reported in Table 2, from which a combined uncertainty lower than 20% of the measured value can be estimated for the out-of-plane displacement measurement.

Table 2
Vision system calibration: average out-of-plane displacements (Z) measured by reference laser transducer and by 3D digital image correlation.

Z_{LASER} (mm)	Z_{DIC} (mm)	SD_{DIC}[a] (mm)	ERR_{ACC}[a] (%)	ERR_{REP}[a] (%)
0.000	0.000	0.000	–	0
0.010	0.009	0.001	10	14
0.020	0.019	0.004	7	18
0.030	0.028	0.006	6	19
0.040	0.037	0.005	8	12
0.050	0.046	0.004	8	8
0.060	0.055	0.004	8	7
0.070	0.067	0.004	4	6
0.080	0.077	0.003	4	4
0.090	0.087	0.005	4	6
0.100	0.098	0.006	3	6
0.110	0.108	0.009	2	8
0.120	0.117	0.007	2	6

[a] SD = standard deviation; ERR_{ACC} = accuracy error; ERR_{REP} = repeatability error.

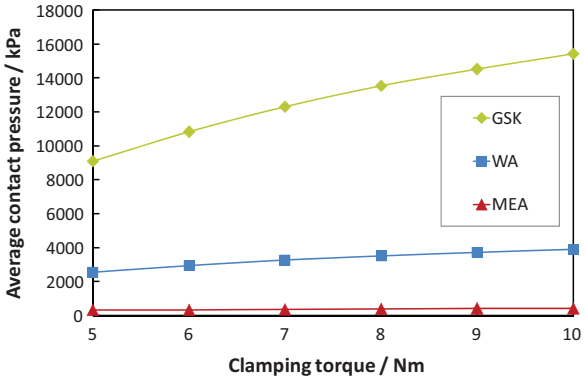

Fig. 8. Average contact pressures measured on the membrane electrode assembly (MEA) and on the sealing gasket (GSK) vs. clamping torque (Cu25 fuel cell). The average value weighted over the whole sensing area (WA) is also shown in the figure.

3. Results

Fig. 8 reports average contact pressures profiles measured on the membrane electrode assembly and on the sealing gasket of the Cu25 fuel cell, as a function of the applied clamping torque. The average value weighted over the whole sensing area is also shown in the figure. The average pressure on the MEA varies from 339 kPa to 429 kPa (Table 3) as the clamping torque is raised from 5 to 10 N m, while on the gasket it increases monotonically up to 16 MPa, with local peaks that exceed the saturation level of the array (20.7 MPa).

Colour-coded pressure contours over the whole contact area of the Cu25 fuel cell are shown in Fig. 9. These pressure maps were obtained by exploiting the full range of the piezoresistive sensor (256 digital levels or 20.7 MPa). In order to better visualize the actual pressure distribution on the MEA, the experimental data

Table 3
Average pressure, standard deviation and uniformity index measured on the MEA (Cu25 cell).

Clamping torque (N m)	Avg. press. (kPa)	Std. dev. (kPa)	Uniformity index (%)
5	339	238	30
6	353	244	31
7	381	256	33
8	396	268	32
9	416	275	34
10	429	280	35

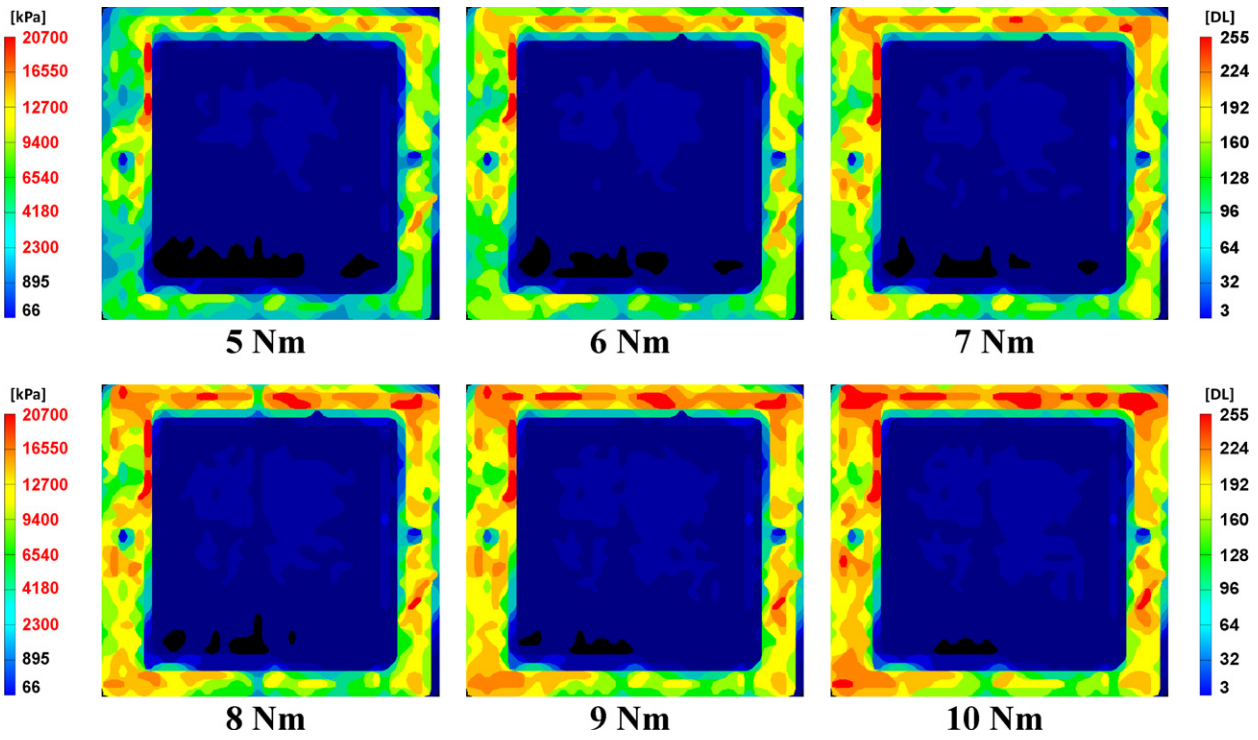

Fig. 9. Colour-coded pressure contours showing pressure distribution measured on the whole sensing area of the Cu25 PEFC at different clamping torques (0–20.7 MPa). Extrapolated values are shown in red colour in the legend. (For interpretation of the references to colour in this figure legend, the reader is referred to the web version of the article.)

have been re-plotted in Fig. 10 by excluding the gasket area and reducing the number of digital levels.

Figs. 11a and 12a show full-field maps of the endplate out-of-plane deformation measured on the Cu25 and Al25 fuel cell, respectively, at 10 N m clamping torque (the two unfitted areas on these images correspond to the threaded holes made into the endplates to allow reactants inlet, see also Fig. 2a). These data were obtained without the gasket and the MEA since further experiments performed by the authors showed that the displacement field on the endplates is not appreciably affected by the presence of the sealing gasket or the membrane electrode assembly. Moreover, this arrangement eliminated the spatial filtering effect produced by the

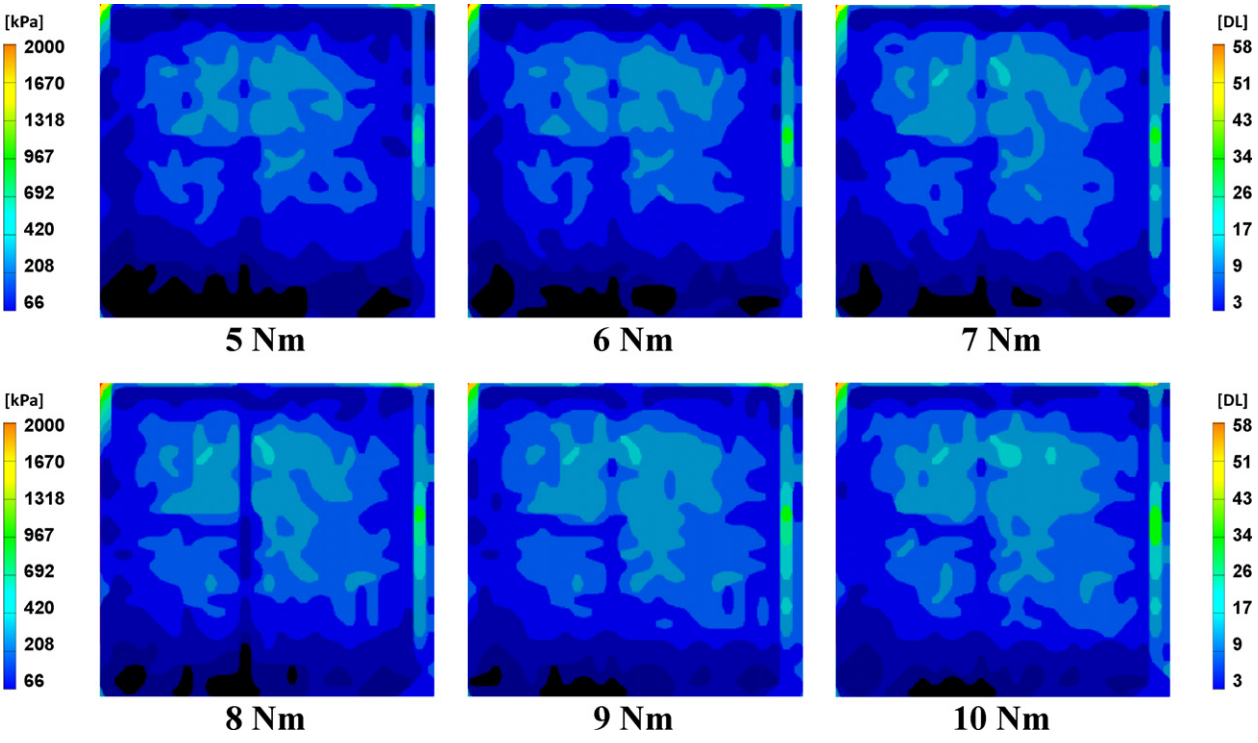

Fig. 10. Colour-coded pressure contours showing pressure distribution measured on the MEA of the Cu25 PEFC at different clamping torques (0–2000 kPa). (For interpretation of the references to colour in this figure legend, the reader is referred to the web version of the article.)

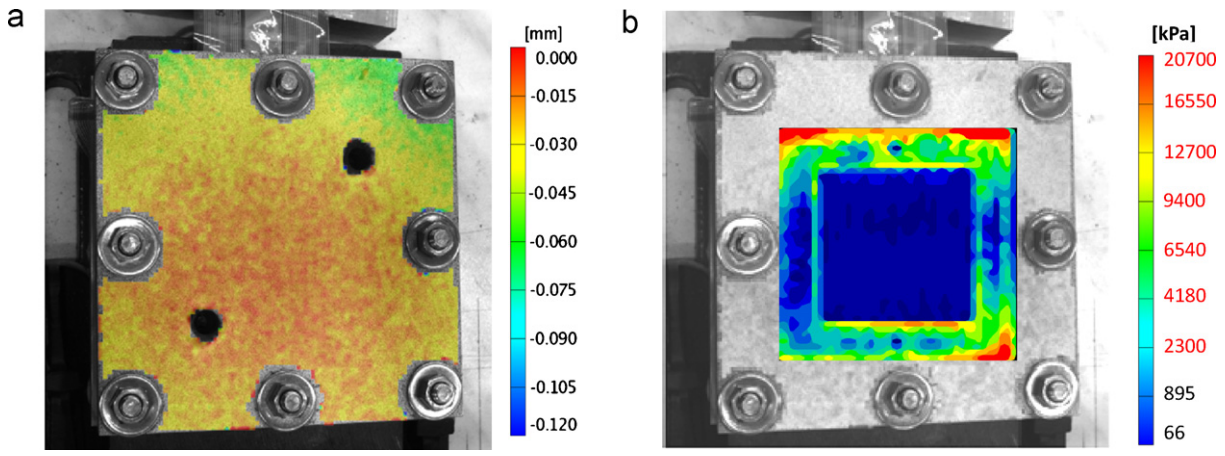

Fig. 11. Simultaneous measurement of endplate deformation and inner pressure distribution on the Cu25 fuel cell without gasket and MEA at 10 N m clamping torque: (a) out-of-plane displacement map; (b) pressure contours map. Extrapolated values are shown in red colour in the legend. (For interpretation of the references to colour in this figure legend, the reader is referred to the web version of the article.)

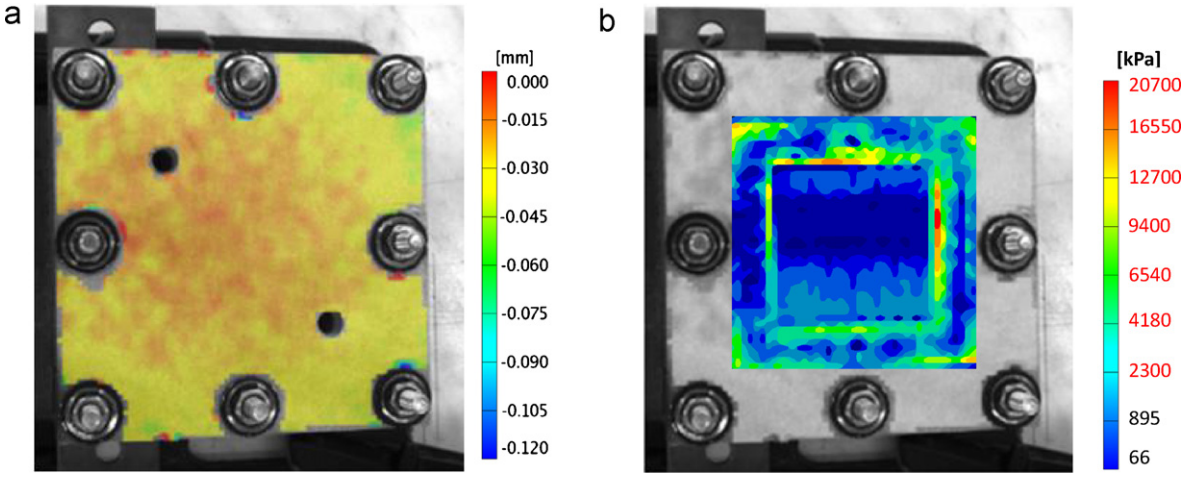

Fig. 12. Simultaneous measurement of endplate deformation and inner pressure distribution on the Al25 fuel cell without gasket and MEA at 10 N m clamping torque: (a) out-of-plane displacement map; (b) pressure contours map. Extrapolated values are shown in red colour in the legend. (For interpretation of the references to colour in this figure legend, the reader is referred to the web version of the article.)

deformable gasket at the interface between the two graphite plates, allowing the effective load path to be better analysed.

Figs. 11b and 12b show the corresponding pressure distribution for the Cu25 and Al25 fuel cell, respectively, obtained in the same configuration as before (measurements were actually performed simultaneously). These figures also allow the relative location of the sensor array with respect to the endplate to be appreciated qualitatively.

Fig. 13 reports average contact pressures profiles measured on the membrane electrode assembly and on the sealing gasket of the Al25 fuel cell, as a function of the applied clamping torque. The average value weighted over the whole sensing area is also shown in the figure. The average pressure on the MEA varies from 836 kPa to 1049 kPa (Table 4) as the clamping torque is raised from 5 to 10 N m, while on the gasket it increases monotonically up to 17.7 MPa, with local peaks that exceed the saturation level of the array (20.7 MPa).

The comparison between normalized pressures on the MEA at 10 N m clamping torque is shown in Fig. 14 for the two assembly configurations (Cu25 and Al25). The normalized pressure was defined as:

$$z = \frac{P - \bar{P}}{\bar{P}} \quad (1)$$

being P the local pressure value and $\bar{P}$ the mean value computed over the MEA area.

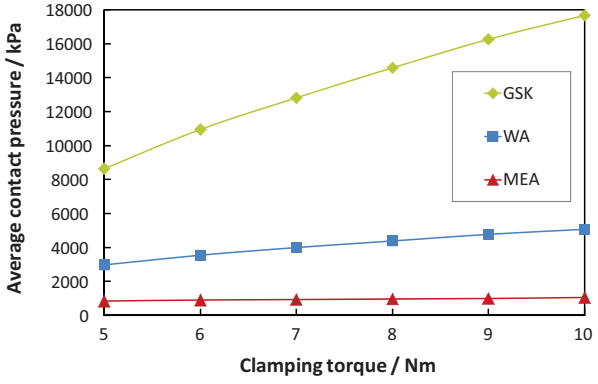

Fig. 13. Average contact pressures measured on the membrane electrode assembly (MEA) and on the sealing gasket (GSK) vs. clamping torque (Al25 fuel cell). The average value weighted over the whole sensing area (WA) is also shown in the figure.

4. Discussion

To achieve good performance in PEFC it is believed that, for a certain cell configuration, an optimum level of the contact pressure on the membrane electrode assembly should be attained [3]. Ideally, the optimum value is to be achieved throughout the fuel cell active

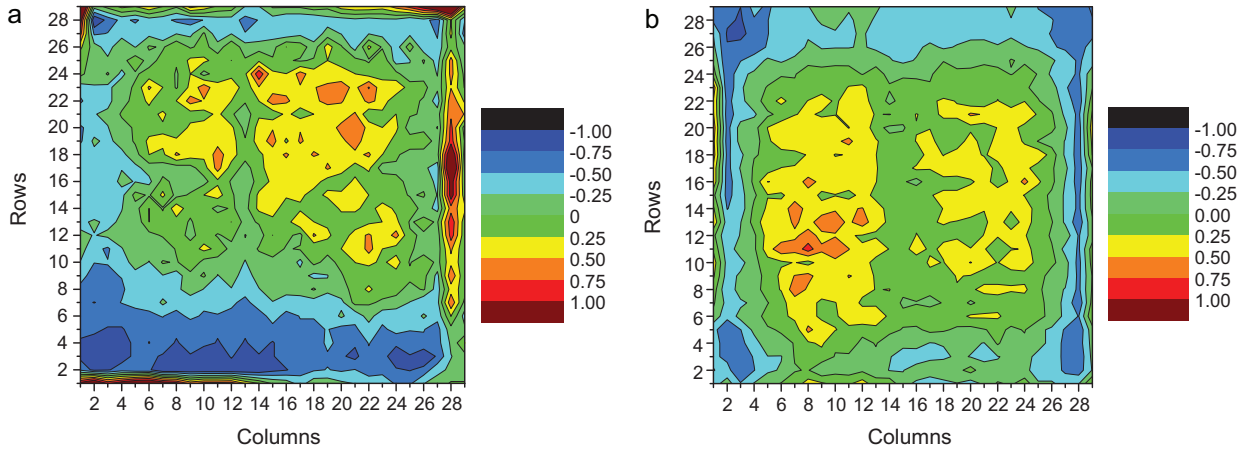

Fig. 14. Surface plots of normalized pressure distributions on the MEA at 10 N m clamping torque: (a) Cu25 PEFC and (b) Al25 PEFC.

area, but actually it can only be achieved in a limited portion of that area because of the point-load design of conventional endplates. Hence, accurate assessment of contact pressure magnitude and distribution on the MEA is still a challenging task for PEFC developers. However, since for a given clamping configuration the pressure distribution on the MEA is thought to be strictly related to the actual curvature assumed by the endplates, endplates deformation should be quantified as well. This task was addressed in the present study, in which a methodology based on the simultaneous measurements of contact pressure magnitude/distribution and endplates deformation has been introduced. The proposed technique allows important features of the complex interaction existing among the several components of the PEFC to be highlighted. Moreover, the use of piezoresistive sensor arrays allowing real-time continuous data acquisition lets some important drawbacks of conventional pressure films to be overcome.

By looking to average pressure profiles measured on the Cu25 cell (Fig. 8), it can be noted that, as the clamping torque is raised from 5 to 10 N m, the pressure level on the MEA displays a slight increase (+25%). In contrast, it increases monotonically up to 16 MPa (+64%) on the sealing gasket, reaching locally very high peaks that exceeded the saturation level of the sensor array (20.7 MPa). Hence the clamping pressure is mainly supported by the gasket which is progressively compressed as the bolts torque is raised up. Since in our case the thicknesses of the MEA and gasket were comparable, the observed behaviour can be easily explained by considering the different Young modulus of carbon paper (5.7 MPa) and PTFE (55 MPa). Otherwise, the relative thickness of the sealing gasket with respect to that of the MEA is expected to play an important role, especially if wearing effects and porosity changes of the gas diffusion layer are taken into account too.

Further information can be gathered by analysing the colour-coded pressure contours reported in Figs. 9 and 10 (Cu25 fuel cell). Even if the flow field channels (having widths of about 1.2 mm) on the graphite plate could not be distinguished due to the limited spatial resolution of the sensor array used to carry out the tests, nevertheless other key features of the contact behaviour can be highlighted. The pressure distribution clearly shows that pressure peaks are localized nearby the peripheral region of the sealing gasket. This behaviour seems to indicate that the endplates bent under load due to the compressive action of the bolts (this aspect will be further examined below with more details).

Table 4
Average pressure, standard deviation and uniformity index measured on the MEA (Al25 cell).

Clamping torque (N m)	Avg. press. (kPa)	Std. dev. (kPa)	Uniformity index (%)
5	836	267	68
6	902	278	69
7	946	281	70
8	982	281	71
9	1012	280	72
10	1049	282	73

Looking at the pressure distribution on the MEA (Fig. 10), it can be observed that the more external region of the contact area seems to remain relatively unloaded as compared to the core one. Hence the MEA is not uniformly loaded, even if the clamping torque is increased. Several factors may contribute to account for the observed behaviour, such as occurrence of manufacturing tolerance and form errors in fuel cell components, thinning of the gasket caused by cyclical cell assembling/disassembling, aging-induced damages on graphite plates. It is interesting to note that measurements carried out by the authors on a 50 cm^2 cell [11] showed an opposite behaviour, with the central region of the MEA that became relatively unloaded as the clamping torque was increased. This apparent inconsistency can be explained by considering the higher deformation of the endplates for the larger cell as well as to the difference in GDL material and gaskets used in the two studies. In fact, a carbon cloth based GDL and an expanded PTFE gasket were used in the former work, while carbon paper GDL and bulk PTFE gasket are used in the current study. In both cases, critical aspects of the load transmission mechanism can be easily brought to light by the use of piezoresistive sensor arrays in the development stage of the fuel cell.

As previously mentioned, pressure distribution measurements performed on the Cu25 cell seem to indicate that the endplate curvature changes as the cell is clamped with progressively higher torques. DIC measurements provide an unambiguous confirmation of this hypothesis, as shown in Fig. 11a. Moreover, by comparing the full-field out-of-plane displacement map with the contact pressure contour measured simultaneously inside the fuel cell (Fig. 11b), a good correlation was found. The fact that the central area occupied by the flow field is clearly visible in the pressure map is symptomatic of the presence of small tolerance errors in the manufacturing of the graphite plate, which are well revealed by the sensor array. Again, the proposed methodology reveals itself valuable in identifying assembling anomalies that eventually might compromise severely the PEFC electro-chemical performance. The results also highlight that the deformation of the endplate cannot be kept perfectly symmetric, due to unavoidable small differences in the assembly mechanism. This was confirmed by either repeating the tests several times or changing the wrenching

sequence: a perfect symmetry was never achieved with the current clamping configuration.

The bundle endplate/current collector of the Al25 cell exhibits a mechanical stiffness that is much higher with respect to the copper endplate of the Cu25 cell. By comparing Figs. 11a and 12a it can be shown that endplate deformation is markedly less pronounced in this case and the pressure distribution more homogeneous (Fig. 12b).

Looking at these results, a more uniform pressure distribution on the MEA is expected when stiffer endplates are employed. This was confirmed by defining a dimensionless uniformity index as follows:

$$U(\%) = \left(1 - \frac{SD}{\bar{P}}\right) \times 100 \quad (2)$$

where SD and $\bar{P}$ are the standard deviation and the mean value of the pressure distribution measured on the MEA. The obtained results are reported in Tables 3 and 4 for the Cu25 and Al25 fuel cells, respectively. The mean pressure on MEA and the uniformity index for the Al25 cell are about 2.45 and 2 times greater than for the Cu25 cell, although absolute pressure variations were comparable in the two cases. This conclusion is also supported by surface plots of normalized pressures computed at 10 N m clamping torque, shown in Fig. 14. As can be observed, the fraction of the MEA where the normalized pressure is in the ±0.5 range (i.e., where P is within ±50% of $\bar{P}$ is appreciably higher for the Al25 cell (Fig. 14b) than for the Cu25 one (Fig. 14a). Moreover, as different studies (see, for example the paper of Chang et al. [10]) already reported that in order to assist the mass transfer from gas channels to the catalyst layers of carbon paper-based MEA, a mean compressive stress between 1000 and 2000 kPa should be attained on the MEA, our study showed that this pressure level can never be reached using the current Cu25 configuration.

Innovative concepts, such as the development of multi-objective endplates topology optimization [13] or the use of composite endplates with pre-curvature [14] can be practicable solutions to improve the uniformity of the pressure distribution on the MEA. In these cases, the proposed methodology might help their experimental validation.

5. Conclusions

PEFC systems technology has now reached the full maturity and the first commercial applications in the field of small energy suppliers or back-up units are expected to be launched on the market in the next few years. The premise for a wide diffusion of this technology mainly depends on two crucial factors: cost reduction and energy efficiency improvement. While the first factor is strongly conditioned by government strategies and possible economies of scale and is therefore susceptible of large cutbacks, the second one presents limited space of improvement, made of small incremental steps.

The present work addresses a problem that has been scarcely investigated in literature, although several studies already suggested that by enhancing the homogeneity of pressure distribution on the MEA better electro-chemical performance could be achieved.

The reported results highlight the effectiveness of the proposed approach, which allowed gaining quantitative data about the correlation between the actual pressure distribution within the fuel cell, the applied external clamping torque and the endplate deformation. It was shown that by increasing endplates stiffness a more efficient load transmission mechanism can be obtained, although other factors, such as gasket/MEA matching and manufacturing tolerances, should be taken into account as well.

The proposed methodology might assist the design of next-generation fuel cells or could be used as a powerful validation tool for detailed finite element models.

Future work directions will try to find evidence about the actual correlation existing between the pressure distribution attained on the MEA using different gasket/GDL thickness ratios and the resulting relevant electrode kinetic parameters of the fuel cell.

Acknowledgments

The authors would like to thank Fabio Irato and Sergio Manera for their helpful assistance in performing the experimental tests.

The work was partially financed under the EU research project “Centro Ricerche Tecna Territorio – PIT 22” POR SICILIA 2000–06 – n. 1999.IT.16.1.PO.011/3.15/5.2.13/0017.

References

[1] W. Vielstich, A. Lamm, H.A. Gasteiger (Eds.), Handbook of Fuel Cells: Fundamentals, Technology and Applications, vols. 1 and 3, Wiley & Sons Inc., New York, 2003.
[2] W.-k. Lee, C.-H. Ho, J.W.V. Zee, M. Murthy, Journal of Power Sources 84 (1999) 45–51.
[3] X. Wang, Y. Song, B. Zhang, Journal of Power Sources 179 (2008) 305–309.
[4] C.Y. Wen, Y.S. Lin, C.H. Lu, Journal of Power Sources 192 (2009) 475–485.
[5] S.J. Lee, C.D. Hsu, C.H. Huang, Journal of Power Sources 145 (2005) 353–361.
[6] L. Zhang, Y. Liu, H. Song, S. Wang, Y. Zhou, S.J. Hu, Journal of Power Sources 162 (2006) 1165–1171.
[7] P. Zhou, C.W. Wu, G.J. Ma, Journal of Power Sources 159 (2006) 1115–1122.
[8] P.H. Chi, S.H. Chan, F.B. Weng, A. Su, P.C. Sui, N. Djilali, International Journal of Hydrogen Energy 35 (2007) 2936–2948.
[9] D. Liu, X. Lai, J. n Ni, L. Peng, S. Lan, Z. Lin, Journal of Power Sources 172 (2007) 760–767.
[10] W.R. Chang, J.J. Hwang, F.B. Weng, S.H. Chan, Journal of Power Sources 166 (2007) 149–154.
[11] R. Montanini, G. Squadrito, G. Giacoppo, Proc. XIX IMEKO World Congress, Lisbon, Portugal, September 6–11, 2009.
[12] R. Montanini, G. Squadrito, G. Giacoppo, in: G. Neri, al. et (Eds.), Sensors and Microsystems, Lecture Notes in Electrical Engineering, Chapter No.: 72, Springer Science+Business Media B.V, Dordrecht, Netherlands, 2011.
[13] P. Lin, P. Zhou, C.W. Wu, Journal of Power Sources 196 (2011) 1222–1228.
[14] H.N. Yu, S.S. Kim, J.D. Suh, D.G. Lee, Composite Structures 92 (2010) 1498–1503.